Development 137, 1887-1896 (2010) doi:10.1242/dev.050526

The miR-143-*adducin3* pathway is essential for cardiac chamber morphogenesis

Dekker C. Deacon[1], Kathleen R. Nevis[1], Timothy J. Cashman[1], Yong Zhou[1], Long Zhao[1], Daniel Washko[1], Burcu Guner-Ataman[1], C. Geoffrey Burns[1,*] and Caroline E. Burns[1,2,*]

SUMMARY

Discovering the genetic and cellular mechanisms that drive cardiac morphogenesis remains a fundamental goal, as three-dimensional architecture greatly impacts functional capacity. During development, accurately contoured chambers balloon from a primitive tube in a process characterized by regional changes in myocardial cell size and shape. How these localized changes are achieved remains elusive. Here, we show in zebrafish that microRNA-143 (miR-143) is required for chamber morphogenesis through direct repression of *adducin3* (*add3*), which encodes an F-actin capping protein. Knockdown of miR-143 or disruption of the miR-143-*add3* interaction inhibits ventricular cardiomyocyte F-actin remodeling, which blocks their normal growth and elongation and leads to ventricular collapse and decreased contractility. Using mosaic analyses, we find that miR-143 and *add3* act cell-autonomously to control F-actin dynamics and cell morphology. As proper chamber emergence relies on precise control of cytoskeletal polymerization, Add3 represents an attractive target to be fine-tuned by both uniform signals, such as miR-143, and undiscovered localized signals. Together, our data uncover the miR-143-*add3* genetic pathway as essential for cardiac chamber formation and function through active adjustment of myocardial cell morphology.

KEY WORDS: microRNA, *miR-143* (*mir143*), Adducin, Zebrafish, Heart development, Organogenesis

INTRODUCTION

Developing organs, including the heart, adopt a characteristic size and shape that is essential for their function. Even subtle perturbations in cardiac architecture can lead to congenital heart defects and, in the most extreme forms, to embryonic lethality (Manner, 2009). Despite the obvious clinical implications, little progress has been made in defining the genetic pathways that drive cardiac morphogenesis.

During development, the heart assembles as a linear tube of myocardial cells that are uniform in shape and size (Auman et al., 2007; Manasek, 1976). This tube then undergoes the concurrent morphogenetic events of looping and chamber ballooning to give rise to the mature organ (Manner, 2009). During looping, the heart tube bends away from the body in a process associated with larger, more elongated cells on the convex side versus smaller, more rounded cells on the concave side (Manasek et al., 1972; Soufan et al., 2006; Taber, 2006). Simultaneously, the cardiac chambers balloon into bean-shaped structures that consist of a convex, greater surface termed the outer curvature (OC) and a concave, lesser surface called the inner curvature (IC) (Auman et al., 2007; de la Cruz and Sanchez-Gomez, 1998; Taber, 2006). As in the bent heart tube, OC chamber myocardial cells are larger and more elongated than their smaller, rounded IC cell counterparts (Auman et al., 2007; Manasek et al., 1972; Meilhac et al., 2004). Thus, the initial differences in cell size and shape of the bending heart tube correspond to the future ICs and OCs of the mature chambers (Christoffels et al., 2000; Taber, 2006). How these localized changes in cell size and shape are achieved to produce accurately contoured chambers remains elusive.

Both extrinsic and intrinsic mechanisms have been shown to affect changes in cell morphology (Auman et al., 2007; Christoffels et al., 2000). The uniformly distributed forces of blood flow and contractility are known to affect chamber formation in zebrafish by either promoting or restricting cell size and elongation, respectively, in the OC (Auman et al., 2007). Intrinsic, regionally expressed markers, such as *Irx5*, *nppa* (*anf*) and *Chisel* (*Smpx*), are found exclusively on the convex side of the bent heart tube and in corresponding OC cells of the mature chamber (Auman et al., 2007; Christoffels et al., 2000). Intriguingly, explanted chick hearts have been shown to bend in culture by a process involving regionalized changes in cell morphology (J. K. Butler, MA thesis, University of Texas, 1952) (Manning and McLachlan, 1990). These data indicate that cell growth and elongation are active events driven by developmental programs intrinsic to the heart. Together, these results support a model in which both genetic programs and physical forces influence the bulging of OC myocardium from the linear heart tube via a process that involves active changes in myocardial cell size and shape (Auman et al., 2007; Manasek et al., 1972; Meilhac et al., 2004; Soufan et al., 2006).

Several lines of experimentation suggest that F-actin dynamics within OC myocytes supply sufficient force to bend the heart tube by promoting cell growth and elongation (Itasaki et al., 1989; Manasek et al., 1972; Taber, 2006; Voronov et al., 2004). Heart tube bending from explanted chick hearts is blocked by the addition of actin polymerization inhibitors (Itasaki et al., 1991; Latacha et al., 2005; Manasek et al., 1972). Moreover, each chamber curvature has been shown to display a unique F-actin distribution in chick: actin fibers retain a circumferential localization in the IC, whereas OC myocytes redistribute their actin filaments in a net-like pattern throughout the cytoplasmic space (Itasaki et al., 1989; Shiraishi et

[1]Cardiovascular Research Center, Massachusetts General Hospital, Harvard Medical School, Charlestown, MA 02129, USA. [2]Harvard Stem Cell Institute, Cambridge, MA 02138, USA.

*Authors for correspondence (gburns@cvrc.mgh.harvard.edu; cburns6@partners.org)

Accepted 25 March 2010

al., 1992). This rearrangement of actin fibers is thought to actively drive cell growth and elongation in OC cells, while their static localization is thought to maintain cell size and circularity in IC cells (Taber, 2006). However, no genetic programs have been reported to regulate F-actin dynamics during chamber emergence.

microRNAs (miRNAs) are known to play important roles in cardiac development and disease (Bartel, 2004; Divakaran and Mann, 2008). These non-coding RNAs bind to target transcripts, inhibit their translation and often cause nonsense-mediated mRNA decay (Bartel, 2009; Giraldez et al., 2006). Binding sequences for individual miRNAs have been predicted based on algorithms that account for nucleotides 2-8 at the 5′ end, referred to as the 'seed sequence' (Bartel, 2009). More recently, studies in zebrafish (Choi et al., 2007) and cultured cells (Baek et al., 2008) have suggested that a major function of miRNAs is to serve as rheostats to fine-tune target mRNA translation.

Here, we show that miR-143 is expressed in the zebrafish heart during cardiac chamber ballooning. Using morpholino knockdown analyses, we find that miR-143 is required for ventricular chamber formation and function. Our studies reveal a primary role for miR-143 in promoting OC myocardial cell growth and elongation via repression of its conserved target, *adducin3* (*add3*), which encodes a cytoskeletal F-actin capping protein. Protection of endogenous *add3* transcripts from miR-143-mediated repression, or mosaic overexpression of *add3* in cardiomyocytes (CMs), leads to a block in cell elongation and F-actin rearrangements. Our findings suggest that Add3 acts in a cell-autonomous manner to regulate cytoskeletal growth and remodeling, a process tightly regulated by miR-143 function.

MATERIALS AND METHODS

Zebrafish lines and maintenance

Zebrafish were maintained under standard conditions. Ethical approval was obtained from the Institutional Animal Care and Use Committees of Massachusetts General Hospital. The following lines were used: *Tg(cmlc2::GFP)*, *Tg(cmlc2::DsRed^{nuc})*, *Tg(flk1::GFP)* and wild-type AB, TuAB and Wik strains.

Northern analysis, in situ hybridization and quantitative PCR

Total RNA was isolated from wild-type (WT) and experimental animals at 48 hpf, 20 μg run on a 15% polyacrylamide TBE-urea gel and then probed with ^{32}P-labeled oligomeric DNA probes complimentary to mature miR-143 or miR-145 as described (Kloosterman et al., 2007).

In situ hybridization was performed as described (Thisse et al., 1993) using digoxygenin-labeled antisense RNA probes to *cmlc2*, *nppa* and *add3*. Probes were synthesized using a DIG RNA Labeling Kit (SP6/T7; Roche). miR-143 in situ hybridizations were performed as described (Wienholds et al., 2005) using 2 pmol of LNA probe with additional EDC fixation steps (Pena et al., 2009). Following in situ hybridization, embryos were embedded in JB-4 plastic resin (Polysciences) and 10 μm sections were cut using a Leica microtome. Double fluorescence in situ hybridization was performed as previously described (Auman et al., 2007; Schoenebeck et al., 2007).

Embryos were injected with either 0.5 mM *MO^{143}* or 0.25 mM *MO^{add3TP}*, collected at 48 hpf, lysed in TRIzol reagent (Invitrogen) and total RNA purified. cDNA was synthesized with random hexamers using Superscript III reverse transcriptase (Invitrogen). cDNA (2 ng) was used to evaluate *add3* expression by real-time quantitative (q) PCR (7900HT Fast Real-Time PCR System, ABI) using forward primer 5′-GCGGCAAGACTTCAACATG-3′ and reverse primer 5′-TTCCCCTTGTTCATCTGCTC-3′. *bactin1* served as an internal control (Burns et al., 2005a).

Immunofluorescence and F-actin staining

Immunohistochemistry was performed as described (Alexander et al., 1998), using primary antibodies against DM-GRASP (zn-8, 1:15 dilution; Developmental Studies Hybridoma Bank, University of Iowa) and α-actinin (1:100; Santa Cruz Biotechnology). Secondary antibodies were obtained from Invitrogen (1:1000). F-actin was visualized with Alexa Fluor 546-conjugated phalloidin (Invitrogen) at 1:75 using an established protocol (Horne-Badovinac et al., 2003). Embryos were mounted in 1% low melting point agarose and imaged using an LS5 confocal microscope (Zeiss).

Morpholino, mimic, plasmid and RNA microinjections

Antisense morpholinos were synthesized as follows (shown 5′ to 3′): multi-blocker miR-143 (*MO^{143}*, CGAGCTACAGTGCTTCATCTCAGA-CTCCCAG); guide Dicer miR-143 (*gDi^{143}*, TACAGTGCTTCATCTCA-GACTCCCA); star Dicer miR-143 (*sDi^{143}*, GTTGACCAGAGATGC-AGCACTGCAC); and target protector morpholino (*MO^{add3TP}*, ACATGA-GAGATGAGTGGTAGATAGA) (Gene Tools). MOs were injected at 0.5-1.0 mM in 1× Danieau medium/1× Phenol Red into the yolk of 1- to 2-cell embryos. A miR-143 Dharmacon mimic was injected at 8-20 μM (Thermo Scientific #C-300611-05). *MO^{143}* and *MO^{add3TP}* were co-injected at 0.16 μM and 0.2 mM, respectively. For plasmid injections, WT embryos were injected with 150 pg/nl of *tol2*-flanked *Tg(cmlc2::add3;cmlc2::GFP)*, *Tg(cmlc2::GFP-2A-add3)* or *Tg(cmlc2::GFP)* circular plasmid DNAs together with 100 pg/nl of transposase RNA.

M-Mode analysis

Short movies were acquired and original software used for their conversion to still-motion mode (M-Mode) images as described (Seguchi et al., 2007). End-systolic ventricular width was measured over a series of cardiac cycles and divided by the end-diastolic ventricular width to yield percentage fractional shortening (FS%).

Microangiography

Microangiography was performed as described (Cheng et al., 2001; Isogai et al., 2001). Approximately 3 nl of a 50% bead solution (0.36 μm fluoresceinated, carboxylated, latex micro-beads, Invitrogen) in double-distilled water/1% BSA was injected through the yolk into the sinus venosus of 36 and 48 hpf embryos mounted in tricane/2% methyl cellulose.

Calcium imaging

One-cell embryos were injected with 1 nl of 1 mM dextran-coupled Calcium Green (MW3000, Molecular Probes). Embryos were incubated in the dark until 48 hpf, at which time the heart was removed, mounted and imaged in Tyrode's medium containing blebistatin to stop physical contraction in the live heart. Fluorescence was imaged on an inverted microscope (Nikon TE2000) and recorded at 800 frames per second using a high-speed CCD camera (CardioCCD-SMQ, RedShirt Imaging, Decatur, GA, USA). Images were analyzed and isochronal maps generated with Metamorph software (Universal Imaging, Downington, PA, USA) as previously described (Milan et al., 2006). The fluorescence intensity in the ventricle and atrium was measured and plotted versus time.

Transmission electron microscopy

Embryos were fixed, dehydrated, embedded, sectioned and imaged as previously described (Majumdar and Drummond, 2000).

Morphometrics and sample sizes

Morphometric analyses were performed on zebrafish hearts after immunostaining with an anti-DM-GRASP antibody. ImageJ software (NIH, http://rsbweb.nih.gov/ij) was used to trace cell outlines and measure surface area and perimeter as described (Auman et al., 2007). Circularity was calculated as a normalized ratio of area (A) to perimeter (P), with a ratio of 1:1 representing a perfect circle (circularity=$4\pi A/P^2$). Using this system, the value distinguishes cell surfaces that are more circular from those that are more elliptical. Cells were selected to be measured based on the clarity of their borders in the *xy* plane of view.

Sample sizes: WT, 147 IC cells and 209 OC cells from six hearts; *MO^{143}*, 185 IC cells and 191 OC cells from six hearts; *MO^{add3TP}*, 124 IC cells and 189 OC cells from five hearts; miR-143 mimic, 171 IC cells and 227 OC cells from eight hearts. Fourteen *Tg(cmlc2::add3,cmlc2::GFP)* mosaic animals were imaged to count 58 GFP$^+$ Add3$^+$ OC cells. Seven *Tg(cmlc2::GFP-2A-add3)* mosaic animals were imaged to count 14 GFP$^+$ Add3$^+$ cells in the OC. Six *Tg(cmlc2::GFP)* embryos were imaged to count

18 GFP$^+$ cells in the OC of control animals. For blastula transplantation: WT, six IC cells and 14 OC cells from two hearts; *MO^{143}*, five IC cells and 11 OC cells from two hearts.

Transplantation

Standard techniques were used to create chimeric embryos at mid-blastula stages (Ho and Kane, 1990). Ten to fifteen blastomeres from uninjected or *MO^{143}*-injected *Tg(cmlc2::GFP)* donors were placed in the margin of WT hosts and developed until 54 hpf, fixed in 4% paraformaldehyde, immunostained with DM-GRASP antibodies, and imaged as described above. No differences in viability were observed between recipients receiving WT or morphant donor cells.

Sensor assay

RNA was synthesized using mMessage Machine (Ambion) and injected at 150 pg/nl (GFP WT or MUT sensor RNA) or 200 pg/nl (DsRed control RNA). miR-143 mimic (#C-300611-05, ThermoFisher Scientific, Lafayette, CO, USA) was injected at 8 μM, whereas control miR-21 (Ambion) was injected at 2 μM. Average pixel intensity for the embryo was quantified in ImageJ, background corrected, and normalized to red control levels as described (Giraldez et al., 2006) (*n*=6 for each group). All statistics were performed using unpaired Student's *t*-tests.

RESULTS

miR-143 is expressed in the heart during cardiogenesis

A large-scale effort to characterize miRNA localization in the zebrafish embryo revealed that miR-143 localizes to the heart at 5 days post-fertilization (dpf) (Wienholds et al., 2005). We more precisely defined the miR-143 expression profile by whole-mount in situ hybridization and first detected transcripts throughout the heart tube at 36-38 hours post-fertilization (hpf), a developmental stage coinciding with the onset of looping and chamber ballooning (Fig. 1A,B). At 48 and 72 hpf, miR-143 became restricted to the ventricle and outflow tract (Fig. 1C-E). At 5 dpf, miR-143 was visualized in plastic sections in the ventricle, outflow region and in an anterior population of extra-cardiac pharyngeal cells (Fig. 1F). High-magnification images revealed miR-143 transcripts throughout the thickness of the ventricular wall (Fig. 1G).

miR-143 is essential for cardiac function

To determine whether miR-143 is required for cardiogenesis, we used an antisense morpholino (*MO^{143}*) to knockdown processing of mature miR-143 (see Fig. S1 in the supplementary material). To confirm that *MO^{143}* efficiently blocks miR-143 biosynthesis, we isolated total RNA from control and *MO^{143}*-injected embryos and performed northern blot analysis (Fig. 2A). Mature miR-143 was visible in control embryos, but absent from morphants. Another miRNA, miR-145, which shares the same primary cistron with miR-143 (Cordes et al., 2009; Thatcher et al., 2008), was present in both samples. We next analyzed heart development in *MO^{143}*-injected *Tg(cmlc2::GFP)* embryos, which express GFP specifically in the myocardium (Burns et al., 2005b). Although the body axes of miR-143 morphants appeared normal at 48 hpf, pericardial edema was apparent (Fig. 2D, black arrowhead). Closer examination revealed contracting, dilated atria, and collapsed ventricles exhibiting severely decreased function (*n*=860/1095) (Fig. 2B-G; see Movies 1 and 2 in the supplementary material). We confirmed the specificity of the *MO^{143}*-induced cardiac defect by injecting two non-overlapping morpholinos, both of which showed loss of miR-143 transcripts by northern analyses and resulted in a gross phenocopy of the cardiac defect (*gDi^{143}*, *n*=80/102; *sDi^{143}*, *n*=160/185) (Fig. 2F and see Fig. S1 in the supplementary material).

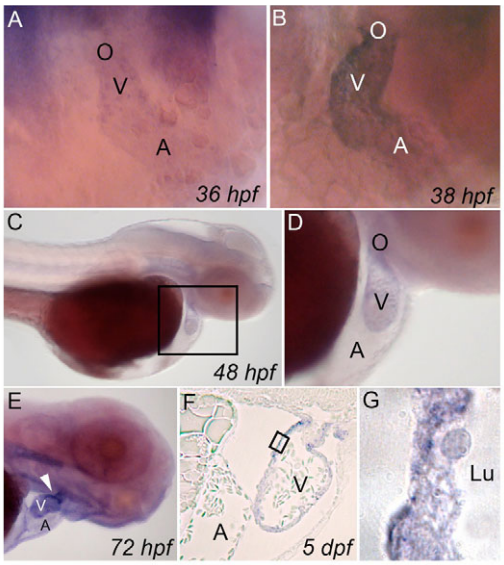

Fig. 1. miR-143 is expressed in the zebrafish embryonic heart. Whole-mount in situ hybridization for miR-143. (**A**,**B**) At 36 and 38 hpf, miR-143 is expressed throughout the heart tube and outflow tract (OFT). Anterior views. (**C**,**D**) At 48 hpf, miR-143 is expressed in the ventricle and OFT. Lateral view (C) and magnification of the heart (D). (**E**) Ventricular miR-143 expression at 72 hpf; OFT expression is high at this stage (arrowhead). Expression is also observed in pharyngeal cells. (**F**) At 5 dpf, transcripts are detected in the ventricle, OFT and in a population of pharyngeal cells. Plastic sections. (**G**) Magnification of the boxed region in F; miR-143 transcripts are detected throughout the ventricular wall. O, outflow tract; V, ventricle; A, atrium; Lu, lumen.

To quantify the output deficiency, end-diastolic and end-systolic dimensions of wild-type (WT) and morphant ventricles were measured with M-Mode software (Seguchi et al., 2007) and a percentage fractional shortening (FS%) was calculated. At 36 hpf, no significant difference in FS% was observed (*MO^{143}*, *n*=8; WT, *n*=5) (Fig. 2G). Microangiography confirmed blood flow in the morphants (*MO^{143}*, *n*=40) (Fig. 2H,J), suggesting proper cardiovascular function. However, at 48 hpf a substantial decrease in FS% was observed (*MO^{143}*, *n*=14; WT, *n*=14) (Fig. 2G), and microangiography revealed restricted blood flow as evidenced by the trapping of fluorescent beads in the yolks and atria (*MO^{143}*, *n*=19) (Fig. 2I,K). These data demonstrate that miR-143 promotes normal ventricular contractility and defines a critical interval for miR-143 function between 36 and 48 hpf.

miR-143 is dispensable for myocardial and endocardial formation, cardiac conduction system development and sarcomere assembly and maintenance

A series of assays was performed to examine the possible causes of diminished ventricular output in *MO^{143}* animals. We examined CM differentiation and proliferation by counting CM nuclei from *Tg(cmlc2::DsRed2nuc)* reporter embryos (Mably et al., 2003) at 72 hpf. No difference in CM number was found in *MO^{143}* hearts compared with controls (WT, *n*=20; *MO^{143}*, *n*=22) (Fig. 3A-C). The endocardium, which was assessed using *Tg(flk1::GFP)* reporter embryos (Jin et al., 2005) (*flk1* is also known as *kdrl* – Zebrafish Information Network), was also found to be present at 48 hpf (*n*=26/31 for morphants; *n*>30 for controls) (Fig. 3D,E). Analysis of calcium flux using a fluorescent indicator showed regular waves

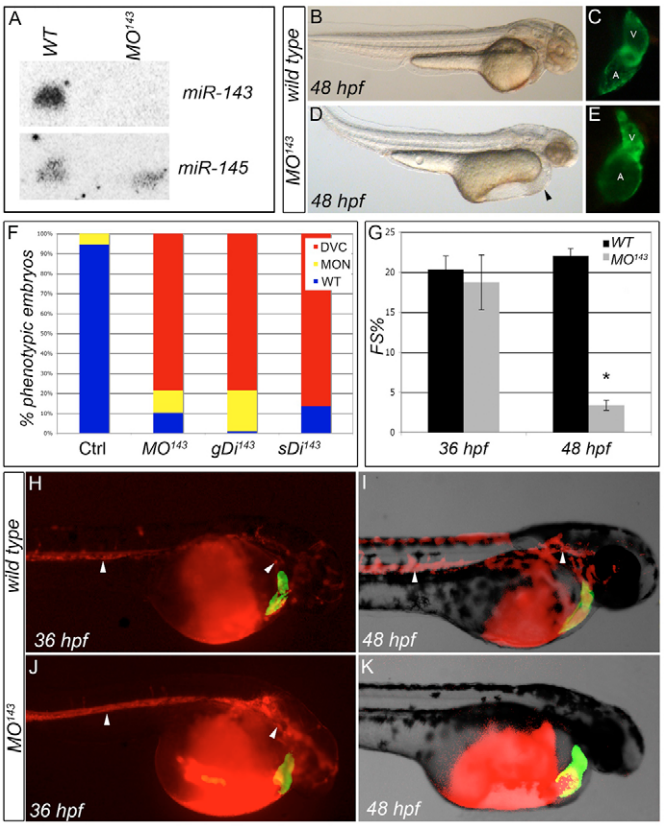

Fig. 2. Inhibition of miR-143 biosynthesis results in structural malformations of the cardiac chambers and decreased cardiac function. (**A**) Northern analysis. No mature miR-143 can be visualized in *MO*^{143} zebrafish embryos, whereas miR-145 expression appears unaltered. (**B-E**) Inhibition of miR-143 biosynthesis results in ventricular collapse and atrial dilation. Lateral views (anterior to the right) are shown of control and *MO*^{143}-injected *Tg(cmlc2::GFP)* embryos at 48 hpf imaged under transmitted (B,D) and fluorescent (C,E) light. Arrowhead in D indicates pericardial edema. (**F-K**) Inhibition of miR-143 compromises ventricular function between 36 and 48 hpf. (F) The percentage of animals with a contractile defect at 48 hpf elicited by three independent morpholinos. DVC, decreased ventricular contractility (red); MON, monster (alive but severely deformed and not accurately scorable for the heart defect; yellow); WT, wild type (blue). (G) Contractility as percentage fractional shortening (FS%) in WT and *MO*^{143} hearts at 36 and 48 hpf. *, P=8.03×10^{-15}; error bars represent ± s.e.m. (H-K) Microangiography of WT and *MO*^{143} embryos at 36 and 48 hpf. Arrowheads indicate circulating beads in the head and trunk. Red, beads; green, myocardium.

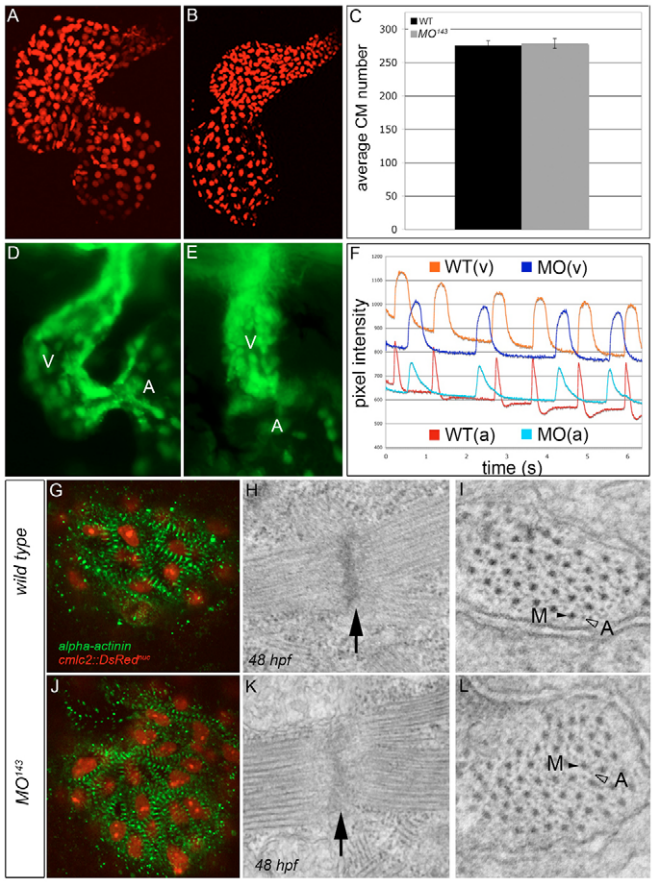

Fig. 3. miR-143 is dispensable for proper myocardial and endocardial cell specification, conduction system development and sarcomere assembly. (**A**,**B**) Flattened confocal images of 72 hpf WT (A) and *MO*^{143} (B) zebrafish hearts carrying a transgene that expresses *DsRed2* in cardiomyocyte (CM) nuclei. (**C**) The average number of total CMs. Error bars represent ± s.e.m. (**D**,**E**) WT (D) and *MO*^{143} (E) hearts at 48 hpf carrying an *flk1::GFP* transgene to highlight the endocardium. The ventricle is shown predominantly. (**F**) Calcium Green fluorescence levels over time in the atria (bottom) and ventricles (top) of 48 hpf WT (blue) and *MO*^{143}-injected (red) embryos. (**G**,**J**) WT and *MO*^{143}-injected *Tg(cmlc2::DsRed*^{nuc}*)* embryos (red nuclei) stained with anti-α-actinin (green) to visualize Z-bands at 48 hpf. (**H**,**I**,**K**,**L**) TEMs of WT and *MO*^{143} ventricles at 48 hpf showing Z-disks (H,K, arrows) and sarcomeric bundles (I,L) with organized myosin (M, black arrowheads) and actin (A, open arrowheads) fibers.

of fluorescence in both WT and *MO*^{143} hearts at 48 hpf (Fig. 3F). Additionally, the normal delay of conduction at the atrioventricular node was preserved in *MO*^{143} animals, as readily observed on a shortened time-scale (not shown). Sarcomere assembly was also found to be normal in morphant ventricles at 48 hpf, as evidenced by the presence of Z-bands visible in α-actinin-stained hearts (Fig. 3G,J) and transmission electron micrographs (TEMs) (Fig. 3H,K). TEMs also showed properly organized myofiber bundles containing myosin and actin filaments (Fig. 3I,L). These data demonstrate that the output defect observed in miR-143 morphants does not result from gross abnormalities in endocardial or myocardial specification, conduction system development or sarcomere assembly and maintenance.

Ventricular OC myocytes fail to grow and elongate in the absence of miR-143

Regionalized changes in cell size and shape have been shown to correlate with chamber morphogenesis (Auman et al., 2007; Manasek et al., 1972; Soufan et al., 2006). To determine whether cell size and shape are altered in the absence of miR-143, we visualized the outlines of myocardial cells in WT and morphant *Tg(cmlc2::GFP)* animals by immunostaining with the zn-8 antibody that recognizes the cell-surface antigen DM-GRASP (Alcama – Zebrafish Information Network) (Beis et al., 2005; Fashena and Westerfield, 1999) (Fig. 4A-I). Confocal images were acquired and CM cell area and circularity were quantified using ImageJ as previously described (Auman et al., 2007). Because the

ventricle does not balloon in morphant animals, the OC and IC were defined as regions distal and proximal to the atrioventricular junction, respectively.

At 48 hpf, both WT and morphant IC cells remained similarly spherical (Fig. 4B,E), showing no observable difference in circularity (Fig. 4J). IC morphant cells were slightly larger than WT cells (P=9.04×10^{-7}), indicating that some cell growth may be achieved in the absence of miR-143. Conversely, WT OC cells appeared larger and substantially more elongated than morphant OC cells, which remained small and circular (P=1.40×10^{-50} and P=1.56×10^{-193}, respectively) (Fig. 4C,F,J,K). These data indicate that miR-143 is crucial for OC cell growth and elongation.

To test the sufficiency of miR-143 in promoting myocardial cell growth and elongation, we analyzed CM size and circularity in embryos overexpressing miR-143 mimic RNA at 48 hpf. miR-143 did not alter cell size or shape in the OC (Fig. 4G-K); however, IC cells were much larger (P=5.17×10^{-20}) and more elongated (P=1.46×10^{-21}) than their WT counterparts (Fig. 4G-K). These findings suggest that although miR-143 is sufficient to aberrantly enlarge and elongate IC cells, it is not capable of hyper-enlarging/extending OC cells.

Since the OC appeared defective in morphant ventricles, we determined whether a conserved marker of OC fate, *natriuretic peptide precursor A* [*nppa*; also known as *atrial natriuretic factor* (*anf*)], was also affected. Interestingly, *MO*^{143} ventricles expressed normal levels of *nppa* (Fig. 4L,M), indicating that morphant OC myocytes display proper regional fate but cannot undergo the cellular processes of growth and elongation.

We next analyzed cell growth and shape of miR-143 morphant cells placed in a WT hemodynamic environment. WT control or *MO*^{143} cells from *Tg(cmlc2::GFP)* donor embryos were transplanted into WT hosts at mid-blastula stages and donor (green) cell morphology was analyzed in the expanded ventricle at 54 hpf (Fig. 4N-P). IC cells were of similar shape and size in WT and morphant donors (Fig. 4Q,R). Conversely, *MO*^{143} OC cells remained smaller and more spherical (P=0.05 and P=3.44×10^{-6}, respectively) (Fig. 4O-R) than WT OC cells, which grew and elongated properly (Fig. 4N,Q,R). Similar to the cell exclusion phenotype displayed by transplanted, non-contractile *ventricular myosin heavy chain* (*vmhc*) mutant cells (Auman et al., 2007), *MO*^{143} cells were sometimes aberrantly extruded from the ventricular wall (Fig. 4P). These results indicate that miR-143 acts downstream of OC cell fate specification to primarily regulate myocardial cell growth and elongation independently of blood flow.

adducin3 is a conserved target of miR-143 repression

To understand the mechanism by which miR-143 regulates cardiac form and function, a list of candidate mRNA targets was generated by mining the TargetScan and PicTar databases (Bartel, 2009; Krek et al., 2005; Lall et al., 2006) for the presence of miR-143 binding sites conserved in 3′ UTRs between chicken and mammals. The hits from each database were cross-referenced and the 34 potential transcripts were analyzed for conservation of the target sequence in zebrafish. From this analysis, a highly conserved miR-143 binding site in the *adducin3 (gamma)* (*add3*) 3′ UTR was identified (Fig. 5A).

Adducin proteins have been shown to form a complex with the fast-growing ends of filamentous actin (F-actin), such that its binding prevents the loss or addition of actin subunits (Matsuoka et al., 2000). As most miRNAs repress their mRNA targets, we

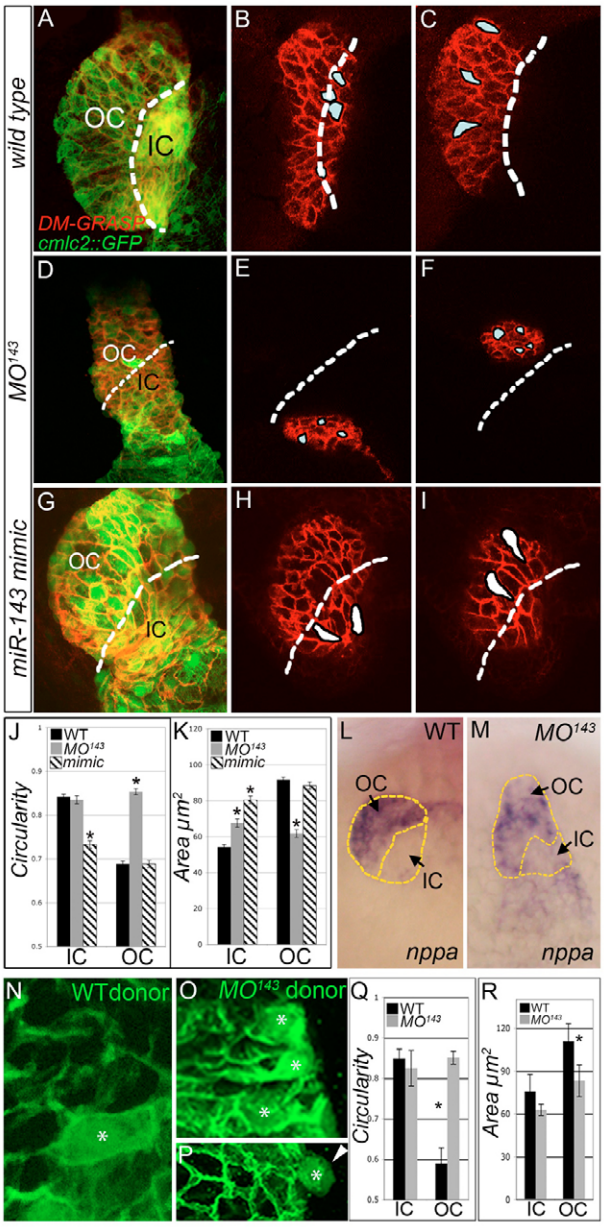

Fig. 4. miR-143 is required and sufficient for CM growth and elongation. (**A-I**) At 48 hpf, WT, *MO*^{143}-injected and miR-143-overexpressing zebrafish embryos carrying a *cmlc2::GFP* transgene (green) were immunostained with anti-DM-GRASP antibodies (red) and imaged by confocal microscopy. Shown are flattened *z*-stacks (A,D,G) and individual sections (B,C,E,F,H,I) from each group. Dashed lines demarcate the approximate outer curvature/inner curvature (OC/IC) boundary based on proximity to the atrioventricular junction. (**J**,**K**) The circularities (J) and areas (K) of cells in the IC and OC of WT, *MO*^{143} and miR-143-overexpressing (mimic) embryos. Asterisk indicates statistical significance compared with WT. (**L**,**M**) In situ hybridization for *nppa* expression in WT (L) and *MO*^{143} (M) animals. The perimeters of the ventricles are highlighted with dashed yellow lines and the OC (*nppa* expressing) and IC (*nppa* non-expressing) populations are indicated. (**N-R**) Chimeric ventricles were derived by transplantation of WT (N,Q,R) or *MO*^{143} (O,P,Q,R) blastula cells carrying the *cmlc2::GFP* transgene. (N-P) Mosaic hearts were immunostained with anti-DM-GRASP to outline cell borders. Representative images of WT (N) and *MO*^{143} cells (O,P, green, *) in the OC. A morphant cell is shown projected from the ventricular wall (P, arrowhead). (Q,R) The average circularity and area for WT and *MO*^{143} cells in the OC and IC.

hypothesized that high Add3 levels might inhibit cellular growth, cellular shape changes and normal contractile force by hyper-stabilizing/polymerizing F-actin.

We utilized four approaches to test whether *add3* is a physiologically relevant target of miR-143 in vivo. We first evaluated *add3* expression during development. At the onset of cardiac looping (~36 hpf), *add3* was predominantly expressed in the head and pronephric ducts, and uniformly within the developing heart tube (Fig. 5B). By 48 hpf, when the cardiac chambers have ballooned and the heart has looped, *add3* transcripts were found throughout both chambers (Fig. 5C). Double-fluorescence in situ hybridization analyses of *add3* and a myocardial marker, *cmlc2* (*myl7* – Zebrafish Information Network), showed colocalization at 36 and 54 hpf (Fig. 5D,E). These data reveal that *add3* is expressed in the correct spatiotemporal domain to be a physiologically relevant target of miR-143.

Second, we analyzed whether the MO^{143} myocardial phenotype is dependent upon miR-143 regulation of *add3*. To specifically disrupt the miR-143-*add3* interaction, we analyzed embryos injected with a target protector morpholino (Choi et al., 2007) complementary to the miR-143 binding site within the *add3* 3′ UTR (MO^{add3TP}) (Fig. 5F). This manipulation should only affect *add3* regulation and leave other miR-143 targets unchanged. Protection of *add3* transcripts from miR-143 phenocopied the MO^{143}-induced ventricular defect (n=75/112) (Fig. 5G,H). The atria became dilated and the ventricles became dysmorphic and showed decreased function (see Movie 3 in the supplementary material). IC cells in MO^{add3TP} animals were of normal size and shape, whereas OC cells failed to grow and elongate ($P=3.73\times10^{-43}$ and $P=3.83\times10^{-37}$, respectively) (Fig. 5I-L). Moreover, MO^{143} and MO^{add3TP} co-injected embryos showed no synergistic affect on CM dimensions compared with either morpholino alone (Fig. 5L), suggesting that miR-143 and *add3* act in the same genetic pathway.

Next, we analyzed the relative abundance of endogenous *add3* transcripts in control and experimentally manipulated embryos by quantitative PCR (Fig. 6A). Overexpression of miR-143 resulted in a ~3-fold decrease in *add3* transcript levels (P=0.0001). Conversely, injection of MO^{143} or MO^{add3TP} showed a ~2-fold increase in *add3* expression levels (P=0.007 and 0.0001, respectively). These data demonstrate that endogenous *add3* transcript levels change in response to increases or decreases in miR-143 activity and reveal that miR-143 exerts a repressive effect on *add3* in vivo.

Finally, we conducted a sensor assay (Flynt et al., 2007; Giraldez et al., 2005; Kloosterman et al., 2007; Kloosterman et al., 2004; Leucht et al., 2008; Yin et al., 2008) to determine whether miR-143 can directly interact with its predicted binding sequence in the *add3* 3′ UTR (Fig. 6B-D). A WT sensor mRNA consisting of GFP fused to the *add3* full-length 3′ UTR (Fig. 6B) was injected into embryos in the presence or absence of the miR-143 mimic RNA or a control miR-21 RNA. *DsRed2* mRNA was co-injected to allow for GFP normalization. At 28 hpf, GFP fluorescence was quantified from each group using ImageJ software and normalized to that of DsRed (Fig. 6C,D) as previously described (Giraldez et al., 2006; Yin et al., 2008). Injection of the WT sensor mRNA alone resulted in

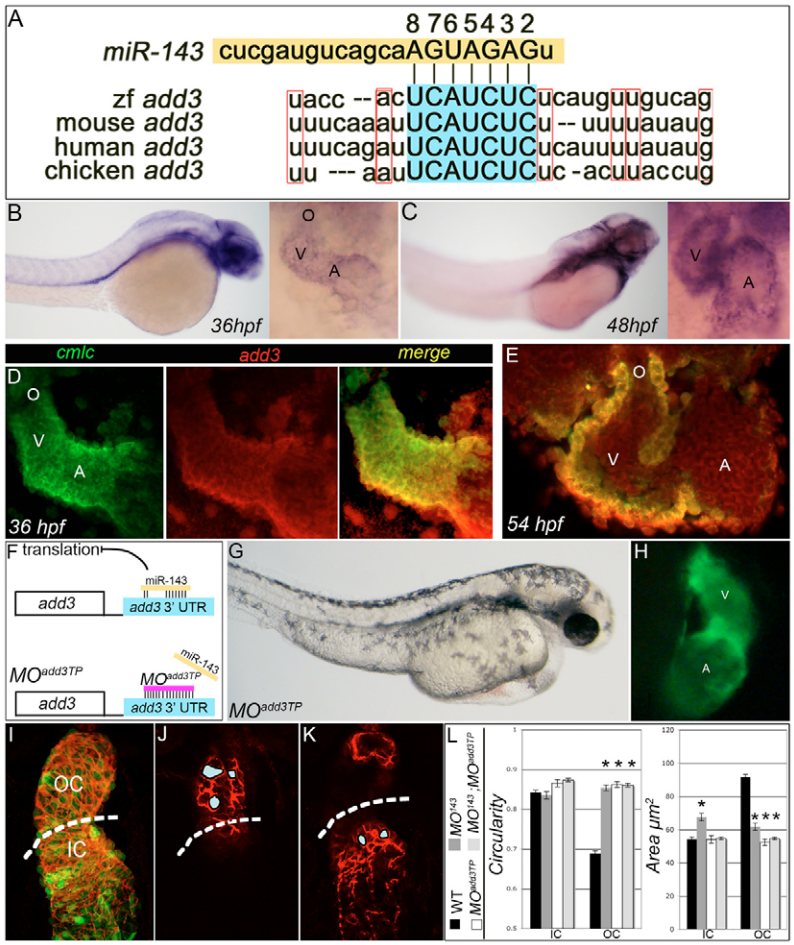

Fig. 5. *add3* is a physiologically relevant target of miR-143 repression. (**A**) The conserved miR-143 seed sequence (2-8) base pairing with its conserved target sequence in the *add3* 3′ UTR. (**B**,**C**) In situ hybridization for *add3*. Left, lateral views; right, high-magnification anterior views of the zebrafish heart. (**D**,**E**) Double-fluorescence in situ hybridization at 36 hpf (D) shows overlapping *cmlc2* (green) and *add3* (red) expression, which is also visible at 54 hpf (E). (**F**) The *add3* target protector morpholino experimental strategy. (**G**,**H**) *Tg(cmlc2::GFP)* embryos were injected with MO^{add3TP} and imaged at 48 hpf under transmitted (G) and fluorescent light (H). Lateral views. As with MO^{143} embryos, MO^{add3TP} animals exhibit ventricular collapse, atrial dilation and compromised function (see Movie 3 in the supplementary material). (**I-K**) Representative sections (J,K) and a flattened *z*-stack (I) of a 48 hpf MO^{add3TP} heart carrying the *cmlc2::GFP* transgene (green) immunostained with anti-DM-GRASP antibody (red). Dashed lines indicate the approximate OC/IC boundary based on the proximity of cells to the atrioventricular junction. (**L**) The average circularity and area of WT, MO^{143}, MO^{add3TP}, and MO^{143} + MO^{add3TP} IC and OC myocytes. Asterisks indicate statistical significance compared with WT; error bars represent ± s.e.m.

bright GFP fluorescence, which was significantly dampened by miR-143 (P=0.002), but not by miR-21 (Fig. 6C). Furthermore, the miR-143-induced dampening was abrogated by co-injection with MO^{143} or MO^{add3TP} (Fig. 6C). These findings were confirmed by quantitative western blot analyses (not shown). Additionally, a single point mutation in the predicted miR-143 binding site blocked the observed GFP silencing by miR-143 (Fig. 6D). These data reveal a specific interaction between miR-143 and the *add3* 3′ UTR and support a model in which ventricular myocardial cell growth and elongation require miR-143-mediated repression of *add3* in vivo.

Add3 functions cell-autonomously to affect F-actin localization

Adducin proteins cap the fast-growing ends of F-actin and stabilize/polymerize the cytoskeleton to preserve cell morphology (Matsuoka et al., 2000). Accordingly, the Adducin-F-actin complex must be disrupted to permit changes in cell size and shape (Fukata et al., 1999). We hypothesized that knockdown of miR-143 results in a net increase in Add3 levels, causing hyper-stabilization of the cytoskeleton and a block in cell growth and elongation.

To test this model, we examined whether F-actin distribution correlates with CM cell shape by visualizing F-actin (phalloidin) localization over the course of chamber formation (see Fig. S2 in the supplementary material). At 24 hpf, when CMs of the linear heart tube are small and circular (Auman et al., 2007), F-actin was localized to the periphery (see Fig. S2A-C in the supplementary material). By 36 hpf, when the heart is beginning to bend, ventricular cells of the future OC showed remodeled F-actin throughout the cytoplasm (see Fig. S2D-F in the supplementary material), whereas future IC cells retained cortical F-actin (see Fig. S2G-I in the supplementary material). By 48 hpf, when the ventricle has fully ballooned, isotropic F-actin fibers were observed throughout the cytoplasm of OC myocytes (see Fig. S2J-L in the supplementary material), whereas F-actin remained peripheral in IC myocytes (see Fig. S2M-O in the supplementary material). These analyses are consistent with previously published findings in chick (Itasaki et al., 1989; Taber, 2006) and suggest that the basic cellular mechanisms driving chamber formation are conserved among vertebrates.

We next examined whether F-actin localization was altered in the OC of MO^{143} and MO^{add3TP} animals. Wild-type OC myocytes showed randomly organized F-actin fibers running throughout the cytoplasm at 54 hpf (n>300 cells from 11 hearts) (Fig. 7A). Conversely, in MO^{143} and MO^{add3TP} OC CMs, F-actin was largely localized to the cortical membrane (MO^{143}, n>300 in eight hearts; MO^{add3TP}, n>100 cells from three hearts) (Fig. 7B,C). These data suggest that unlike WT CMs, which show dynamic F-actin rearrangements, morphant CMs retain F-actin at the cortex.

We next tested whether overexpressing *add3* in CM clones could promote a cell-autonomous block in cell growth, elongation and F-actin redistribution in an environment in which hemostatic pressures are normal. A transgene carrying two *cmlc2* myocardial promoters driving either *GFP* or *add3* expression in opposing orientations (Fig. 7D) was injected and the resulting mosaic animals were stained with phalloidin and anti-DM-GRASP. Control animals were injected with a similar construct expressing GFP alone. Control CMs (GFP alone) were larger and more elongated than those overexpressing Add3 (P=4.9×10^{-5} and P=4×10^{-3}, respectively) (Fig. 7E,F). Whereas abundant cytoplasmic F-actin fibers were observed in elongated control cells (Fig. 7G,H), F-actin showed a strong circumferential orientation in Add3-overexpressing CMs (n=205 cells) (Fig. 7I-N). Similar to MO^{143} transplanted cells (Fig. 4O), 50% of the Add3-overexpressing cells were extruded from the ventricular wall (n=102/205) (Fig. 7K-N). These results suggest that *add3* acts autonomously within the CM lineage to affect F-actin distribution, cell growth and elongation via a process that is independent of alterations in blood pressure. Together, our data uncover the miR-143-*add3* genetic pathway and show that it is essential for chamber formation through direct regulation of F-actin cytoskeletal dynamics.

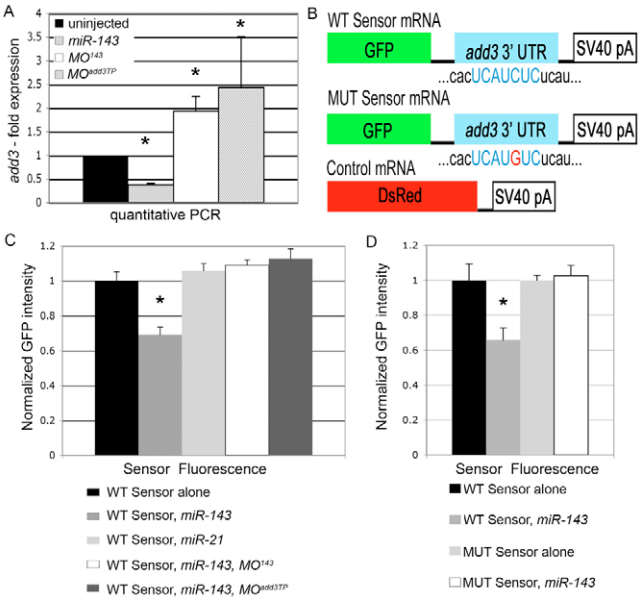

Fig. 6. miR-143 binds to the *add3* 3′ UTR and represses translation in vivo. (**A**) qPCR analysis showing fold changes in *add3* transcript levels in zebrafish embryos injected with miR-143, MO^{143} or MO^{add3TP} as compared with WT (uninjected). (**B**) The mRNAs that were co-injected for the sensor assay. For the mutant (MUT) sensor, the wild-type cytosine was converted to a guanine (highlighted in red). (**C**,**D**) Quantification of normalized GFP florescence from injected embryos imaged at 28 hpf (not shown). Error bars represent ± s.e.m. Asterisk indicates statistical significance compared with WT.

DISCUSSION

Heart looping and chamber ballooning are vital morphogenetic events in cardiac development, with minor perturbations leading to substantial structural and functional abnormalities. Alterations in cytoskeletal dynamics have been suggested to actively drive cardiac morphogenesis by promoting regional changes in cell size and shape (Taber, 2006). Here, we identify and connect the miR-143-*add3* genetic pathway to alterations in F-actin arrangements. To our knowledge, these data provide the first link between a developmental program and the cytoskeletal rearrangements needed for chamber emergence.

Although the mechanism by which IC and OC regional information is established is poorly understood, studies in chick and zebrafish suggest that both intrinsic and extrinsic factors are at play (J. K. Butler, MA thesis, University of Texas, 1952) (Auman et al., 2007; Manning and McLachlan, 1990). Using zebrafish mutants, myocyte contraction has been shown to promote circularity, whereas blood flow has been shown to act as an opposing force, promoting cell elongation (Auman et al., 2007). Specifically, *weak atrium* (*wea*; *atrial myosin heavy chain*; *myh6*)

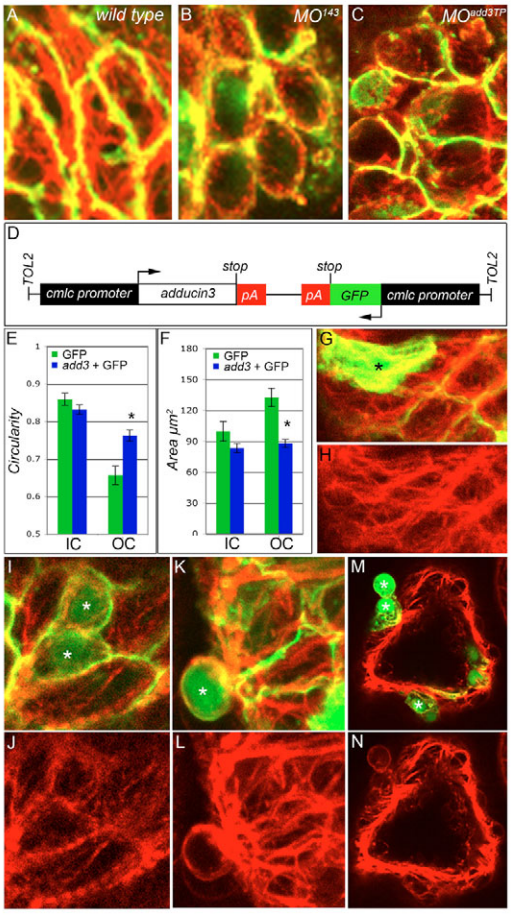

Fig. 7. Add3 functions cell-autonomously to affect F-actin localization. (**A-C**) Flattened *z*-stacks showing phalloidin (red) and anti-DM-GRASP (green) labeling of 48 hpf WT, MO^{143} and MO^{add3TP} zebrafish cardiomyocytes within the OC. (**D**) The construct used to overexpress GFP and *add3* (no 3′ UTR). (**E**,**F**) Cell circularity (E) and area (F) in mosaic hearts. Add3-overexpressing OC myocytes are statistically more circular (blue bar) than OC CMs labeled with GFP alone (green bar). *, *P*=0.00045. Error bars represent ± s.e.m. (**G-N**) Samples of the raw data used to generate the bar charts in E and F. Asterisks indicate GFP^+ cells. (G-L) Head-on view of the ventricular OC. (M,N) Cross-section through the ventricle. (G) Merged confocal image showing WT GFP^+ cells (green) and F-actin distribution (red). (H) Same image as in G but showing phalloidin staining alone. Abundant intracellular F-actin fibers can be seen in elongated GFP^+ OC cells. (I,K,M) Merged confocal images showing *add3*-overexpressing GFP^+ cells (green) and F-actin distribution (red). (J,L,N) The same images as in I,K,M but showing phalloidin staining alone. (I,J) Intracellular fibers are more visible in elongated WT cells than in *add3*-overexpressing neighbors (green). (K-N) Approximately half of the *add3*-overexpressing cells are extruded from the ventricular wall and show obvious cortical F-actin localization as compared with their WT (GFP^-) neighbors.

mutants lack ventricular blood flow and show small CMs with a highly circular morphology. Although these cellular defects are reminiscent of the miR-143 knockdown, the most striking and important difference between the phenotypes is expression of *nppa*. *wea* mutants fail to maintain normal levels of *nppa* in the ventricular chamber, suggesting that blood flow is required for maintaining OC chamber fate. MO^{143} animals, by contrast, express normal levels of *nppa* in the ventricle, but fail to redistribute their actin cytoskeleton. These findings indicate that the blood flow observed at 36 hpf in miR-143 morphants is strong enough to maintain OC regional information and suggest that the defect in chamber morphogenesis lies downstream of cell fate decisions.

Transcriptional initiation of miR-143 commences as the linear heart tube undergoes chamber emergence. Whereas transcription factors such as Hand1, Nppa and Chisel are regionally enriched in emerging OC cells (Christoffels et al., 2000), *nppa* is upregulated in future OC cells prior to cell elongation in zebrafish (Auman et al., 2007). This suggests that regionalized genetic signals, such as *nppa*, create inherent differences among the initially similar cells of the linear heart tube before overt cell size and shape changes occur. These early transcriptional differences might subsequently result in alternative susceptibilities to evenly distributed cues, such as genetic signals or physical forces. Although the mechanism by which the uniformly distributed miR-143 transcript exerts a regional effect on cell size and elongation during chamber emergence is unclear, our data support a role for miR-143 in globally repressing new Add3 protein production.

Two recent reports provide evidence that miR-143 regulates smooth muscle (SM) cell phenotypic switching based on data drawn from expression studies, cell culture experiments and a post-natal arterial injury model (Cordes et al., 2009; Xin et al., 2009). Both studies demonstrate that miR-143 is expressed in mouse aortic SM cells on embryonic day 9.5, consistent with a role for miR-143 in SM biology. However, miR-143 is also expressed much more robustly in progenitor cells of the cardiac crescent on embryonic day 7.5, 2 days prior to SM differentiation, and very highly in all myocardial and endocardial cells of the linear heart tube 1 day prior to SM differentiation. As SM precursors and differentiated cells are not observed in the zebrafish heart until 60 hpf and 21 dpf, respectively (Grimes et al., 2006), a potential SM deficiency cannot explain the profound defect that is evident in MO^{143} embryos by 48 hpf. Moreover, these expression data in mouse support an SM-independent role for miR-143 during cardiogenesis. Although mice deficient for miR-143 are viable and display no cardiac abnormalities (Xin et al., 2009), our zebrafish miR-143 loss-of-function data suggest that other programs might compensate for the absence of miR-143 during murine development. Thus, in addition to a role in SM biology, our findings show that myocardial miR-143 acts to drive the morphogenetic events of heart ontogeny by autonomously regulating cytoskeletal dynamics.

The most compelling argument that a primary function for miR-143 is to regulate myocyte growth and elongation is the identification of a cytoskeletal component, Add3, as one of its required targets. In agreement with our findings, *add3* transcripts have been shown to be 2-fold more abundant in adult SM samples from *miR-143;miR-145* double-knockout mice (Xin et al., 2009). In these studies, miR-143 and miR-145 were shown to actively repress numerous transcripts involved in actin dynamics. Interestingly, two additional miRNAs, miR-1 and miR-133, were recently shown to predominantly target actin-related and actin-binding proteins of the sarcomere in skeletal muscle (Mishima et al., 2009). Since Adducin proteins are known to alter actin cytoskeletal dynamics, Add3 represents an attractive target for converting both uniform and localized genetic signals into precise cell growth and shape changes.

One model for chamber emergence can be envisioned based on the collective results from a variety of model organisms. The linear heart tube consists of smaller, more circular cells that show polymerized F-actin at the periphery. In order for the chamber

myocardium to balloon from the tube, OC CMs must break down their actin cytoskeleton to allow cell growth and elongation, a process that is dependent upon fine-tuning of Add3 function. We hypothesize that miR-143 acts throughout the heart tube to limit the production of new, intracellular Add3 protein, thus providing one level of Add3 regulation. Concomitantly, we speculate that other regionalized signals, such as a kinase (Fukata et al., 1999), might act to post-translationally promote the dissociation of Add3 from F-actin, thereby allowing the cytoskeleton to be redistributed throughout the cell. In the absence of miR-143 function, continued Add3 production might overwhelm other modes of post-translational regulation, leading to sustained Add3-actin complex formation and cytoskeletal polymerization. Discerning whether miR-143 acts in concert with other regionalized factors to influence cell morphology will be vital to appreciating the full role of the miR-143-*add3* pathway in cardiac morphogenesis and, possibly, disease.

Acknowledgements
We thank Daniela Panakova, Andreas Werdich, Jeffrey Winterfield, David Milan, Heather Kolpa, Mary McKee and members of the Iain Drummond laboratory for technical assistance. M-Mode analysis software was kindly provided by Seiji Takashima. Electron microscopy was performed at the Microscopy Core of the Center for Systems Biology, which is supported by an Inflammatory Bowel Disease Grant DK43351 and a Boston Area Diabetes and Endocrinology Research Center Award DK57521. The zn-8 antibody developed by Bill Trevarrow was obtained from the Developmental Studies Hybridoma Bank under the auspices of the NICHD and maintained by the University of Iowa, Department of Biological Sciences, Iowa City, IA 52242, USA. This work was supported by a Basil O'Connor Award from the March of Dimes and by the Cardiovascular Research Center at Massachusetts General Hospital.

Competing interests statement
The authors declare no competing financial interests.

Supplementary material
Supplementary material for this article is available at
http://dev.biologists.org/lookup/suppl/doi:10.1242/dev.050526/-/DC1

References
Alexander, J., Stainier, D. Y. and Yelon, D. (1998). Screening mosaic F1 females for mutations affecting zebrafish heart induction and patterning. *Dev. Genet.* **22**, 288-299.
Auman, H. J., Coleman, H., Riley, H. E., Olale, F., Tsai, H. J. and Yelon, D. (2007). Functional modulation of cardiac form through regionally confined cell shape changes. *PLoS Biol.* **5**, e53.
Baek, D., Villen, J., Shin, C., Camargo, F. D., Gygi, S. P. and Bartel, D. P. (2008). The impact of microRNAs on protein output. *Nature* **455**, 64-71.
Bartel, D. P. (2004). MicroRNAs: genomics, biogenesis, mechanism, and function. *Cell* **116**, 281-297.
Bartel, D. P. (2009). MicroRNAs: target recognition and regulatory functions. *Cell* **136**, 215-233.
Beis, D., Bartman, T., Jin, S. W., Scott, I. C., D'Amico, L. A., Ober, E. A., Verkade, H., Frantsve, J., Field, H. A., Wehman, A. et al. (2005). Genetic and cellular analyses of zebrafish atrioventricular cushion and valve development. *Development* **132**, 4193-4204.
Burns, C. E., Traver, D., Mayhall, E., Shepard, J. L. and Zon, L. I. (2005a). Hematopoietic stem cell fate is established by the Notch-Runx pathway. *Genes Dev.* **19**, 2331-2342.
Burns, C. G., Milan, D. J., Grande, E. J., Rottbauer, W., MacRae, C. A. and Fishman, M. C. (2005b). High-throughput assay for small molecules that modulate zebrafish embryonic heart rate. *Nat. Chem. Biol.* **1**, 263-264.
Cheng, S. H., Chan, P. K. and Wu, R. S. (2001). The use of microangiography in detecting aberrant vasculature in zebrafish embryos exposed to cadmium. *Aquat. Toxicol.* **52**, 61-71.
Choi, W. Y., Giraldez, A. J. and Schier, A. F. (2007). Target protectors reveal dampening and balancing of Nodal agonist and antagonist by miR-430. *Science* **318**, 271-274.
Christoffels, V. M., Habets, P. E., Franco, D., Campione, M., de Jong, F., Lamers, W. H., Bao, Z. Z., Palmer, S., Biben, C., Harvey, R. P. et al. (2000). Chamber formation and morphogenesis in the developing mammalian heart. *Dev. Biol.* **223**, 266-278.
Cordes, K. R., Sheehy, N. T., White, M. P., Berry, E. C., Morton, S. U., Muth, A. N., Lee, T. H., Miano, J. M., Ivey, K. N. and Srivastava, D. (2009). miR-145 and miR-143 regulate smooth muscle cell fate and plasticity. *Nature* **460**, 705-710.
de la Cruz, M. V. and Sanchez-Gomez, C. (1998). Straight tube heart. Primitive cardiac cavities vs. primitive cardiac segments. In *Living Morphogenesis of the Heart* (ed. M. de la Cruz and R. R. Markwald), pp. 85-98. Birkhäuser: Boston.
Divakaran, V. and Mann, D. L. (2008). The emerging role of microRNAs in cardiac remodeling and heart failure. *Circ. Res.* **103**, 1072-1083.
Fashena, D. and Westerfield, M. (1999). Secondary motoneuron axons localize DM-GRASP on their fasciculated segments. *J. Comp. Neurol.* **406**, 415-424.
Flynt, A. S., Li, N., Thatcher, E. J., Solnica-Krezel, L. and Patton, J. G. (2007). Zebrafish miR-214 modulates Hedgehog signaling to specify muscle cell fate. *Nat. Genet.* **39**, 259-263.
Fukata, Y., Oshiro, N., Kinoshita, N., Kawano, Y., Matsuoka, Y., Bennett, V., Matsuura, Y. and Kaibuchi, K. (1999). Phosphorylation of adducin by Rho-kinase plays a crucial role in cell motility. *J. Cell Biol.* **145**, 347-361.
Giraldez, A. J., Cinalli, R. M., Glasner, M. E., Enright, A. J., Thomson, J. M., Baskerville, S., Hammond, S. M., Bartel, D. P. and Schier, A. F. (2005). MicroRNAs regulate brain morphogenesis in zebrafish. *Science* **308**, 833-838.
Giraldez, A. J., Mishima, Y., Rihel, J., Grocock, R. J., Van Dongen, S., Inoue, K., Enright, A. J. and Schier, A. F. (2006). Zebrafish MiR-430 promotes deadenylation and clearance of maternal mRNAs. *Science* **312**, 75-79.
Grimes, A. C., Stadt, H. A., Shepherd, I. T. and Kirby, M. L. (2006). Solving an enigma: arterial pole development in the zebrafish heart. *Dev. Biol.* **290**, 265-276.
Ho, R. K. and Kane, D. A. (1990). Cell-autonomous action of zebrafish spt-1 mutation in specific mesodermal precursors. *Nature* **348**, 728-730.
Horne-Badovinac, S., Rebagliati, M. and Stainier, D. Y. (2003). A cellular framework for gut-looping morphogenesis in zebrafish. *Science* **302**, 662-665.
Isogai, S., Horiguchi, M. and Weinstein, B. M. (2001). The vascular anatomy of the developing zebrafish: an atlas of embryonic and early larval development. *Dev. Biol.* **230**, 278-301.
Itasaki, N., Nakamura, H. and Yasuda, M. (1989). Changes in the arrangement of actin bundles during heart looping in the chick embryo. *Anat. Embryol. (Berl.)* **180**, 413-420.
Itasaki, N., Nakamura, H., Sumida, H. and Yasuda, M. (1991). Actin bundles on the right side in the caudal part of the heart tube play a role in dextro-looping in the embryonic chick heart. *Anat. Embryol. (Berl.)* **183**, 29-39.
Jin, S. W., Beis, D., Mitchell, T., Chen, J. N. and Stainier, D. Y. (2005). Cellular and molecular analyses of vascular tube and lumen formation in zebrafish. *Development* **132**, 5199-5209.
Kloosterman, W. P., Wienholds, E., Ketting, R. F. and Plasterk, R. H. (2004). Substrate requirements for let-7 function in the developing zebrafish embryo. *Nucleic Acids Res.* **32**, 6284-6291.
Kloosterman, W. P., Lagendijk, A. K., Ketting, R. F., Moulton, J. D. and Plasterk, R. H. (2007). Targeted inhibition of miRNA maturation with morpholinos reveals a role for miR-375 in pancreatic islet development. *PLoS Biol.* **5**, e203.
Krek, A., Grun, D., Poy, M. N., Wolf, R., Rosenberg, L., Epstein, E. J., MacMenamin, P., da Piedade, I., Gunsalus, K. C., Stoffel, M. et al. (2005). Combinatorial microRNA target predictions. *Nat. Genet.* **37**, 495-500.
Lall, S., Grun, D., Krek, A., Chen, K., Wang, Y. L., Dewey, C. N., Sood, P., Colombo, T., Bray, N., Macmenamin, P. et al. (2006). A genome-wide map of conserved microRNA targets in C. elegans. *Curr. Biol.* **16**, 460-471.
Latacha, K. S., Remond, M. C., Ramasubramanian, A., Chen, A. Y., Elson, E. L. and Taber, L. A. (2005). Role of actin polymerization in bending of the early heart tube. *Dev. Dyn.* **233**, 1272-1286.
Leucht, C., Stigloher, C., Wizenmann, A., Klafke, R., Folchert, A. and Bally-Cuif, L. (2008). MicroRNA-9 directs late organizer activity of the midbrain-hindbrain boundary. *Nat. Neurosci.* **11**, 641-648.
Mably, J. D., Mohideen, M. A., Burns, C. G., Chen, J. N. and Fishman, M. C. (2003). heart of glass regulates the concentric growth of the heart in zebrafish. *Curr. Biol.* **13**, 2138-2147.
Majumdar, A. and Drummond, I. A. (2000). The zebrafish floating head mutant demonstrates podocytes play an important role in directing glomerular differentiation. *Dev. Biol.* **222**, 147-157.
Manasek, F. J. (1976). *Heart Development: Interactions Involved in Cardiac Morphogenesis*. New York: Elsevier North-Holland.
Manasek, F. J., Burnside, M. B. and Waterman, R. E. (1972). Myocardial cell shape change as a mechanism of embryonic heart looping. *Dev. Biol.* **29**, 349-371.
Manner, J. (2009). The anatomy of cardiac looping: a step towards the understanding of the morphogenesis of several forms of congenital cardiac malformations. *Clin. Anat.* **22**, 21-35.
Manning, A. and McLachlan, J. C. (1990). Looping of chick embryo hearts in vitro. *J. Anat.* **168**, 257-263.
Matsuoka, Y., Li, X. and Bennett, V. (2000). Adducin: structure, function and regulation. *Cell. Mol. Life Sci.* **57**, 884-895.
Meilhac, S. M., Esner, M., Kerszberg, M., Moss, J. E. and Buckingham, M. E. (2004). Oriented clonal cell growth in the developing mouse myocardium underlies cardiac morphogenesis. *J. Cell Biol.* **164**, 97-109.

Milan, D. J., Giokas, A. C., Serluca, F. C., Peterson, R. T. and MacRae, C. A. (2006). Notch1b and neuregulin are required for specification of central cardiac conduction tissue. *Development* **133**, 1125-1132.
Mishima, Y., Abreu-Goodger, C., Staton, A. A., Stahlhut, C., Shou, C., Cheng, C., Gerstein, M., Enright, A. J. and Giraldez, A. J. (2009). Zebrafish miR-1 and miR-133 shape muscle gene expression and regulate sarcomeric actin organization. *Genes Dev.* **23**, 619-632.
Pena, J. T., Sohn-Lee, C., Rouhanifard, S. H., Ludwig, J., Hafner, M., Mihailovic, A., Lim, C., Holoch, D., Berninger, P., Zavolan, M. et al. (2009). miRNA in situ hybridization in formaldehyde and EDC-fixed tissues. *Nat. Methods* **6**, 139-141.
Schoenebeck, J. J., Keegan, B. R. and Yelon, D. (2007). Vessel and blood specification override cardiac potential in anterior mesoderm. *Dev. Cell* **13**, 254-267.
Seguchi, O., Takashima, S., Yamazaki, S., Asakura, M., Asano, Y., Shintani, Y., Wakeno, M., Minamino, T., Kondo, H., Furukawa, H. et al. (2007). A cardiac myosin light chain kinase regulates sarcomere assembly in the vertebrate heart. *J. Clin. Invest.* **117**, 2812-2824.
Shiraishi, I., Takamatsu, T., Minamikawa, T. and Fujita, S. (1992). 3-D observation of actin filaments during cardiac myofibrinogenesis in chick embryo using a confocal laser scanning microscope. *Anat. Embryol. (Berl.)* **185**, 401-408.
Soufan, A. T., van den Berg, G., Ruijter, J. M., de Boer, P. A., van den Hoff, M. J. and Moorman, A. F. (2006). Regionalized sequence of myocardial cell growth and proliferation characterizes early chamber formation. *Circ. Res.* **99**, 545-552.
Taber, L. A. (2006). Biophysical mechanisms of cardiac looping. *Int. J. Dev. Biol.* **50**, 323-332.
Thatcher, E. J., Bond, J., Paydar, I. and Patton, J. G. (2008). Genomic organization of zebrafish microRNAs. *BMC Genomics* **9**, 253.
Thisse, C., Thisse, B., Schilling, T. F. and Postlethwait, J. H. (1993). Structure of the zebrafish snail1 gene and its expression in wild-type, spadetail and no tail mutant embryos. *Development* **119**, 1203-1215.
Voronov, D. A., Alford, P. W., Xu, G. and Taber, L. A. (2004). The role of mechanical forces in dextral rotation during cardiac looping in the chick embryo. *Dev. Biol.* **272**, 339-350.
Wienholds, E., Kloosterman, W. P., Miska, E., Alvarez-Saavedra, E., Berezikov, E., de Bruijn, E., Horvitz, H. R., Kauppinen, S. and Plasterk, R. H. (2005). MicroRNA expression in zebrafish embryonic development. *Science* **309**, 310-311.
Xin, M., Small, E. M., Sutherland, L. B., Qi, X., McAnally, J., Plato, C. F., Richardson, J. A., Bassel-Duby, R. and Olson, E. N. (2009). MicroRNAs miR-143 and miR-145 modulate cytoskeletal dynamics and responsiveness of smooth muscle cells to injury. *Genes Dev.* **23**, 2166-2178.
Yin, V. P., Thomson, J. M., Thummel, R., Hyde, D. R., Hammond, S. M. and Poss, K. D. (2008). Fgf-dependent depletion of microRNA-133 promotes appendage regeneration in zebrafish. *Genes Dev.* **22**, 728-733.